Research Article

Received: 12 October 2018 Revised: 5 December 2018 Accepted article published: 10 December 2018 Published online in Wiley Online Library:

(wileyonlinelibrary.com) DOI 10.1002/jctb.5902

Magnetic sugarcane bagasse composite for atrazine and fluoride removal

Toledo J Helen,[a,b] Blanco-Flores Alien,[c,d] Lopez-Téllez Gustavo,[b] Vilchis-Nestor Alfredo R,[b*] Nubia Arteaga-Larios[d] and Israel Rodríguez-Torres[d]

Abstract

BACKGROUND: The present investigation focuses on the synthesis and application of a magnetic adsorbent material formed by the agro-industrial waste sugarcane bagasse (SCB). Its application in the removal of fluoride and atrazine demonstrates its properties as a potential adsorbent material for the treatment of contaminated wastewater.

RESULTS: The synthesis method proved to be simple and reproducible. The presence and distribution of magnetite and fluoride on the surface of the material were studied by characterization techniques (SEM, EDX, FTIR-ATR). Several specific functional groups were identified which may interact with atrazine and fluoride molecules in the adsorption process. Kinetic results indicated that second- and pseudo-second-order model fitted better for the fluoride and atrazine adsorption processes, respectively. The adsorption processes took place by chemisorption onto heterogeneous surfaces. Isotherm data fitted better to the Langmuir–Freundlich model in both systems; therefore, the process took place by a combination of mechanisms. Cellulose and lignin from sugarcane bagasse contribute in the adsorption process, while magnetite not only improve performance of composite for the removal of the chemical species tested, but also achieve a simple separation process via magnetic interactions' with a common magnet. The adsorption capacities of the composites were 0.5036 mg g^{-1} for fluoride and 40.11 mg g^{-1} for atrazine.

CONCLUSION: The synthesis of the magnetic composite is simple and generates a material that is easy to manipulate and isolate after the process. The affinity of the composite with atrazine is greater than with fluoride; however, the composite can be used in systems with low concentration.

Keywords: magnetite nanoparticles; sugarcane bagasse; atrazine; fluoride

INTRODUCTION

The three most common forms of iron oxides in nature are magnetite (Fe_3O_4), maghemite (γ-Fe_2O_3) and hematite (α-Fe_2O_3).[1] Magnetite is composed of Fe^{2+}, Fe^{3+} and O^{2-} species packaged in an inverse spinel structure, where O^{2-} ions forming a face-centered cubic lattice, and iron cations occupy interstitial sites.[2]

Magnetite is a magnetic mineral that can be found in nature[3] A synthetic form of magnetite can be produced by different simple methods with a high degree of purity.[4] These methods allow control of magnetite form and size. Nanoparticles of magnetite (MNP) with size <10–20 nm exhibit a form of superparamagnetism.[1] In the presence of a low external magnetic field, nanoparticles tend to exhibit a high magnetization response, which is gradually lost with distance from the magnetic field. This property is characteristic of superparamagnetic materials.[5] Some of the most relevant applications include (but are not limited to): magnetic recording, (photo) catalysis, pigments, ferrofluids, contrast agent for magnetic resonance imaging, drug delivery, adsorption support, anti-tumoral agent and bioseparation.[6] Although magnetite has been used as absorbent material for fluoride removal,[7] and for other applications,[8] usually it is found as part of composites.[9] Magnetite composites have been used in biomedical applications,[10] catalysis,[11] removal of heavy metals,[12,13] pesticides,[14] and organic compounds,[15,16] and radioactive species.[17]

Lignocellulosic materials, such as those found in agro-industrial waste, have proven to be a good alternative as supports to obtain composite materials due to their abundance and low cost.[14] The use of waste materials obviously is attractive due to their contribution in reducing the costs of their disposal, therefore contributing to environmental protection.[18] Various agricultural wastes have been explored as low-cost adsorbents, including sugarcane bagasse (SCB).[19] This residue, in its natural form, has been shown to have capacity for removal of heavy metals,[20] halogens such as fluoride,[21] and organic molecules such as dyes.[22] A magnetic modified SCB was prepared by Yu *et al.*[19] to study its adsorption

* *Correspondence to: V-N Alfredo R, Centro Conjunto de Investigación en Química Sustentable UAEM-UNAM, (CCIQS), Carretera Toluca-Atlacomulco km 14.5, Unidad El Rosedal, Toluca, Estado de México, C.P. 50200, México. E-mail: arvilchisn@uaemex.mx*

a *Posgrado en Ciencia de Materiales, Facultad de Química, Universidad Autónoma del Estado de México Paseo Colón y Tollocan, Toluca, México*

b *Centro Conjunto de Investigación en Química Sustentable UAEM-UNAM, (CCIQS), Toluca, México*

c *División de Ingeniería Mecánica, Tecnológico de Estudios Superiores de Tianguistenco, Santiago de Tianguistenco, México*

d *Instituto de Metalurgia – Facultad de Ingeniería, Universidad Autónoma de San Luis Potosí, San Luis Potosí, México*

and desorption of Pb^{2+} and Cd^{2+}. Those experiments showed that the prepared magnetic sorbent had good adsorption performances for heavy metal ions, including high adsorption capacity and rapid adsorption rate. To the best of our knowledge, this kind of composite has not yet been applied to the removal from aqueous solutions of fluoride or atrazine, two pollutants that have been found to alter water quality, representing a risk for the aquatic environment and human health.

Fluoride was routinely added to drinking water because small concentrations of it could be helpful for teeth care. However, a high concentration can be dangerous to human health:[23] dental fluorosis is a sign that fluoride concentration, in the human body, has reached harmful levels.[24] Therefore, high concentrations of this halogen in water should be considered an alarming problem.

Some pesticides, including atrazine, are applied and marketed without any restriction in some countries.[25] Atrazine has been prohibited in Europe since 2010 due to its toxicity. However, it can still be found as noxious waste.[26] On the one hand, atrazine is associated with birth defects[27] and a significant increase in the prevalence of small-for-gestational-age (SGA) babies in humans.[28] On the other, it causes an oestrogenic effect in sexually mature female European quail[29] and is considered an endocrine disruptor on fish.[30]

Several techniques have been used for atrazine and fluoride removal, some of which can be expensive[31] or polluting.[32] Adsorption is an excellent alternative to be used for water decontamination processes since it is low-cost, ecofriendly and easy to implement from laboratory level to industrial scale. Therefore, many different kinds of materials and composites have been used as adsorption materials in processes for fluoride and atrazine removal. A laminated Yttrium-based nanocomposite with high surface area prepared for fluoride removal had an adsorption capacity calculated by the Langmuir isotherm model of 31.0 mg g^{-1}.[33] Chen *et al.*[34] prepared a novel tri-metal nanocomposite by a co-precipitation process. They studied the process at three different temperatures with a maximum adsorption capacity of 47.2 mg g^{-1} at 35 °C. Atrazine removal by natural and H_2SO_4- and NaOH-modified bentonite was reported by Ajala *et al.*[35], giving removal capacities of 76.92, 125.0 and 111.1 mg g^{-1}, respectively. Zeolites and activated carbon (C) are the most proven materials, with or without modification, for atrazine removal, but a new generation of materials has increasingly being used for this task. Metal organic frameworks ZIF-8, UiO-66 and UiO-67 were applied by Akpinar *et al.*[36] with capacities of 6.78, 2.57, 10.96 mg g^{-1}, respectively. Removal of fluoride and atrazine by magnetic materials also has been reported by Dewage *et al.*[37] and Ali *et al.*[38] In the first case MNP were dispersed on Douglas fir biochar to make a composite for fluoride ion removal using magnetic separation, giving a Langmuir maximum capacity of 9 mg g^{-1}. In the second case, an iron nanoparticles composite delivered a maximum adsorption capacity of 12.2 μg g^{-1}.

Many industries use the adsorption process for treating effluents to remove organic and inorganic pollutants,[39] so the demand for low cost and environmental friendly adsorbent materials is evident. Therefore, the purpose of the present research is to study the feasibility of utilizing a SCB magnetic biocomposite (MBo) as a low-cost adsorbent material for fluoride and atrazine removal. Adsorption kinetics were studied, and desorption of iron ions from the composite, during the adsorption process, was analyzed and quantified. This parameter is significant because a high concentration of iron in water could become another environmental pollution problem. MBo were prepared by a co-precipitation process to load MNP on the surface of the bagasse. The materials were characterized by Fourier transform infrared (FTIR), scanning and transmission electron microscopy (SEM and TEM), and X-ray diffraction (XRD).

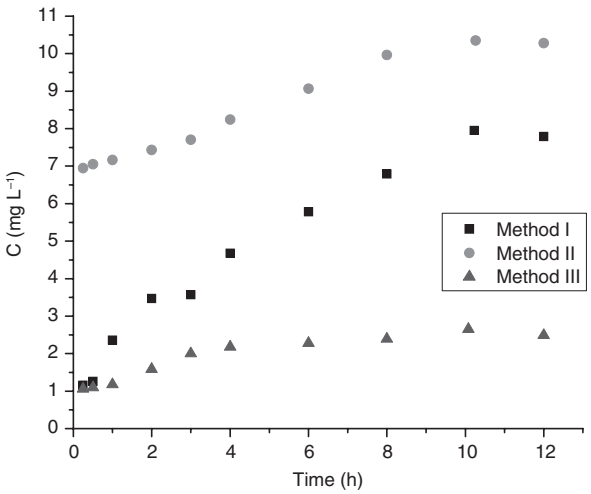

Figure 1. Desorption of Fe from MB_O synthesized by three methods as a function of time (10 mg of MB_O in 5 mL of water at room temperature, stirred over 24 h).

MATERIALS AND METHODS

Reagents

The chemical reagents used in this study were analytical grade, were purchased from Sigma-Aldrich, México and used as received. NaOH; C_2H_5OH; NH_4OH, $FeCl_3 \cdot 6H_2O$ and $FeCl_2 \cdot 4H_2O$ Atrazine was obtained from SYFATEC S.A. de C.V. (Tlanepantla, México) and was used without further purifications. All necessary dilutions were done with deionized water. The working standard solution of fluoride (Thermo Fisher Scientific) was used for the fluoride adsorption experiments.

Synthesis of MNP

The MNP were synthesized by the conventional co-precipitation method.[6] In a typical synthesis: 50 mL of 0.1 mol L^{-1} $FeCl_3$ and 50 mL of 0.05 mol L^{-1} $FeCl_2$ were mixed for 30 min under mechanical stirring in nitrogen atmosphere. Then, 50 mL of 3.5 mol L^{-1} NaOH was added drop-wise under stirring and constant inert atmosphere. The color of the reaction changed immediately but was continually stirred for 1 h, until the reaction was completed. Then a black precipitate containing MNP was separated using a magnet. MNP were washed repeatedly with deionized water and dried.

Preparation of SCB

Natural SCB was obtained from a local juice center in Veracruz, Mexico. The material was sun-dried for 5 days, followed by milling and sieving process through 40–50 μm. The SCB was pretreated in order to avoid possible contaminants, sugars and wax by washing with a C_2H_5OH solution at 10% v/v for 24 h, at room temperature and magnetic agitation. Then the SCB was filtered and dried before use and labeled as B_O.

Magnetic sugarcane bagasse (MB_O) preparation

MB_O was synthesized according to three methods:

Method I

First, a 50 mL $FeCl_3$ (0.1 mol L^{-1}) solution and 50 mL $FeCl_2$ (0.05 mol L^{-1}) were mechanically stirred in a nitrogen atmosphere

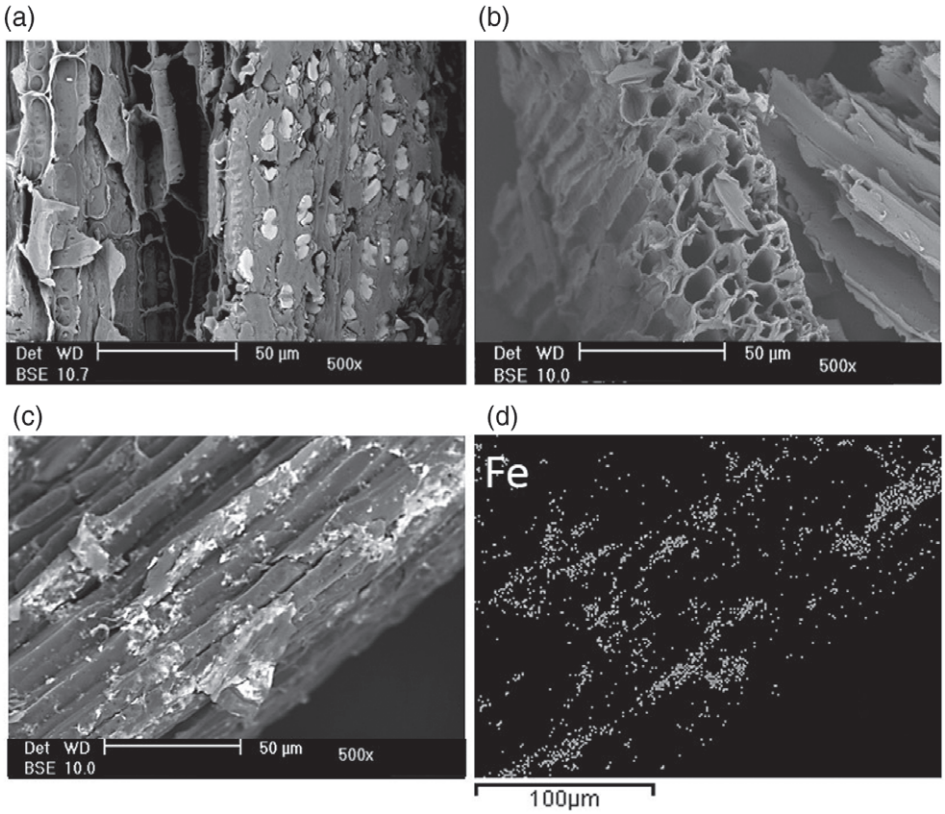

Figure 2. (a) Representative SEM micrographs of natural SCB; (b) treated bagasse B_O; (c) magnetic bagasse MB_O; and (d) EDS chemical mapping of Fe on the MB_O, scale bar = 100 µm.

for 30 min. Then, 2 g B_O was added, the mixture was stirred for another 30 min and the nitrogen atmosphere was maintained. Finally, 50 mL NaOH solution (3.5 mol L^{-1}) was added drop-wise to the mixture, while maintaining mechanical stirring and nitrogen atmosphere.

Method II

First, 50 mL $FeCl_3$ (0.05 mol L^{-1}) solution and 50 mL $FeCl_2$ (0.025 mol L^{-1}) were stirred in a nitrogen atmosphere. Then, 2 g B_O was added and the mixture was stirred for 30 min. Finally, 50 mL NaOH solution (1.75 mol L^{-1}) was added drop-wise to the mixture.

Method III

First, 50 mL $FeCl_3$ (0.1 mol L^{-1}) solution and 50 mL $FeCl_2$ (0.05 mol L^{-1}) were stirred in a nitrogen atmosphere. Then, 4 g B_O was added and the mixture was stirred for 30 min. Finally, 50 mL NaOH solution (3.5 mol L^{-1}) was added drop-wise to the mixture mixture, while maintaining mechanical stirring and nitrogen atmosphere.

In the three methods, the color of bulk solutions changed from orange to black immediately. Mixtures were stirred at 80 °C for 30 min. The MB_O was washed with distilled water and with EDTA solution (0.1 mol L^{-1}) to remove the absorbed iron ions, and then with distilled water to neutralize pH.[40] Washed MB_O was oven-dried at 50° and stored until further use.

Desorption of Fe as a function of time

Desorption experiments of Fe were conducted under static conditions by the batch equilibrium technique, by adding 10 mg MB_O (synthesized by the three methods mentioned above) to 5 mL deionized water with constant stirring at room temperature. At 0.25, 0.5, 1, 2, 4, 6, 7, 8, 12, 16, 20 and 24 h, the composite MB_O was isolated with a magnet. Metal content in the suspensions were determined using an atomic absorption spectrometer Philips model PV9100X with a hollow cathode lamp, and a deuterium background corrector using an air–acetylene flame.

Characterization

The material phases were identified by XRD analysis performed on a Bruker D8 Advance X-ray diffractometer equipped with a CuK radiation source (Karlsruhe, Germany). The nitrogen adsorption–desorption isotherms of the cellulosic support and the composite were determined on an ASAP 2024 Micromeritics device (Georgia, USA), in order to determinate the surface area, pore volume and average pore size. A JEOL (Akishima, Japan) microscope model JEM2100 operated at an accelerating voltage of 200 kV with a LaB_6 filament was used to produce TEM micrographs. The surface morphology was investigated by SEM using a Philips XL-30 (Amsterdam, Netherlands) equipped with a Tungsten gun. In addition, energy-dispersive X-ray spectroscopy (EDX) analyses were carried out in order to obtain chemical composition maps of the different observed sample zones. To elucidate the functional groups present in atrazine, bagasse and the composite after and before the adsorption process, FTIR spectra were recorded in the 4000 to 400 cm^{-1} region at room temperature by a Bruker (model Tensor-27) FTIR-ATR infrared spectrometer (Ettlingen, Germany). X-ray photoelectron spectroscopy (XPS) wide and narrow spectra were acquired on a JEOL (Akishima, Japan) device model JPS-9200.

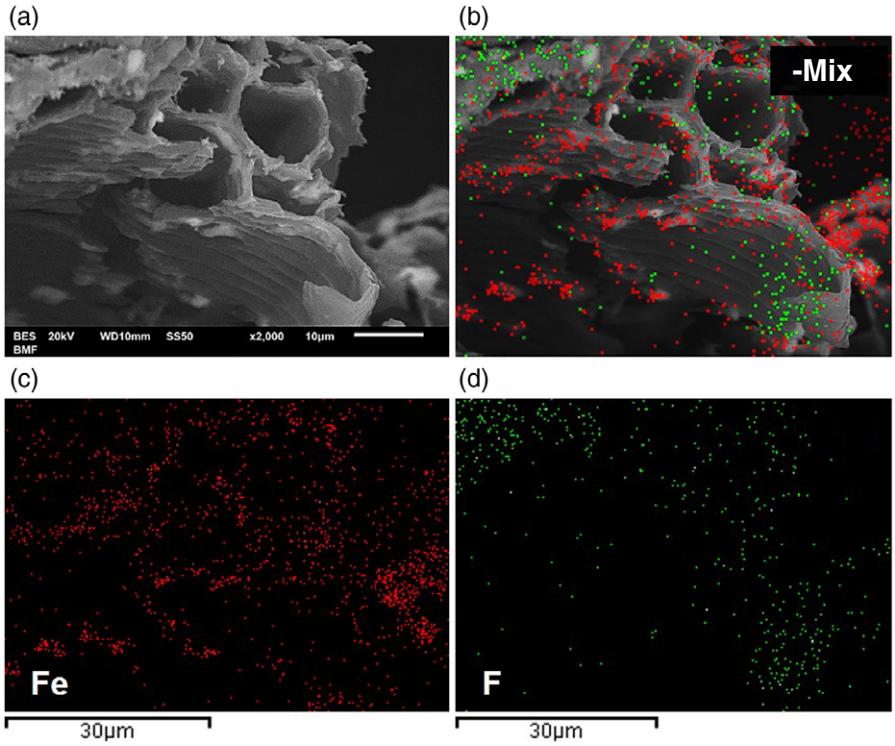

Figure 3. (a) SEM micrograph of MB_O after F adsorption; (b) EDS chemical mapping of the Fe and F on the MB_O after F adsorption, scale bar = 30 µm; (c) and (d) Individual EDS maps showing Fe and F distribution respectively, after the adsorption process.

Adsorption as a function of time

Adsorption experiments of atrazine were conducted under static conditions by the batch equilibrium technique by adding specified volumes of MB_O to 5 mL of 30 mg L^{-1} pesticide solutions with constant stirring at room temperature. At 0.25, 0.5, 1, 2, 4, 6, 7, 8, 12, 16, 20 and 24 h after contact, MB_O were separated from the liquid phase (supernatant) by a magnetic field. The pH values of the solutions were between 6.5 and 7.5. The concentrations in the suspensions were determined by a spectrophotometer (UV–visible Perkin Elmer Lambda 10) at 220 nm.

The fluoride kinetic experiments were carried out at a concentration of 3 mg L^{-1} with 1 g MB_O in 200 mL of the solution over a 24 h time interval. The pH values were between 6.8 and 7.09. At certain time intervals, an aliquot of this solution was taken, and the fluoride concentrations were quantified with a selective ion electrode for fluorine, from Thermo Scientific Orion Model 9609BNWP. The ionic strength was controlled with a buffer solution to remove interfering ions.

All data were analyzed using several mathematical kinetic models: pseudo-first-order [Eqn (1)], pseudo-second-order [Eqn (2)] and second-order [Eqn (3)]. The model-fitting and graphics were accomplished using ORIGIN 8.0 software.

$$q_t = q_e\left(1 - e^{-k_1 t}\right) \tag{1}$$

$$q_t = \frac{k_2 q_e^2 t}{1 + k_2 q_e t} \tag{2}$$

$$q_t = \frac{1}{\beta}\ln(\alpha\beta) + \frac{1}{\beta}\ln t \tag{3}$$

where q_t and q_e (mg g^{-1}) are the adsorption capacity of the adsorbent at equilibrium and at time t theoretical and experimental, respectively; k_1 (h^{-1}) and k_2 (mg g^{-1} h^{-1}) are the constant rate coefficients for the pseudo-first and pseudo-second order models, respectively; and α (mg g^{-1} h^{-1}) and β (g mg^{-1}) are the initial adsorption rate, and the activation energy for chemisorption, respectively.[41]

Adsorption isotherms

The adsorption isotherms of atrazine on MB_O were determined under the same kinetic conditions. Solutions at different concentrations were prepared, ranging from 10 to 100 mg L^{-1}. Afterwards; 5 mL of each solution were individually agitated with MB_O at the equilibrium time established previously. Next, the mixtures were separated and the solutions were analyzed by a UV-visible spectrophotometer. Fluoride solutions were prepared at a range of concentrations (1–30 mg L^{-1}), and 10 mL of each were put in contact with MB_O materials, and stirred for the equilibrium time at room temperature. Then concentrations of fluoride in the liquids were determined.

The amounts of adsorbed atrazine and fluoride per gram of adsorbent material were calculated and a plot of q_e as a function of C_e was built. The experimental equilibrium adsorption data were tested using the two-parameter Freundlich, Langmuir, Temkin and Dubini–Radushkevich isotherm equations, and the three-parameter Langmuir–Freundlich (SIP) equation.

RESULTS AND DISCUSSION

The three magnetic materials were prepared under the same conditions of temperature, contact time and stirring velocity, and solutions were prepared with the same water and reagents. All conditions were maintained as constant as much as possible. By reducing the concentrations of the reactive solutions from

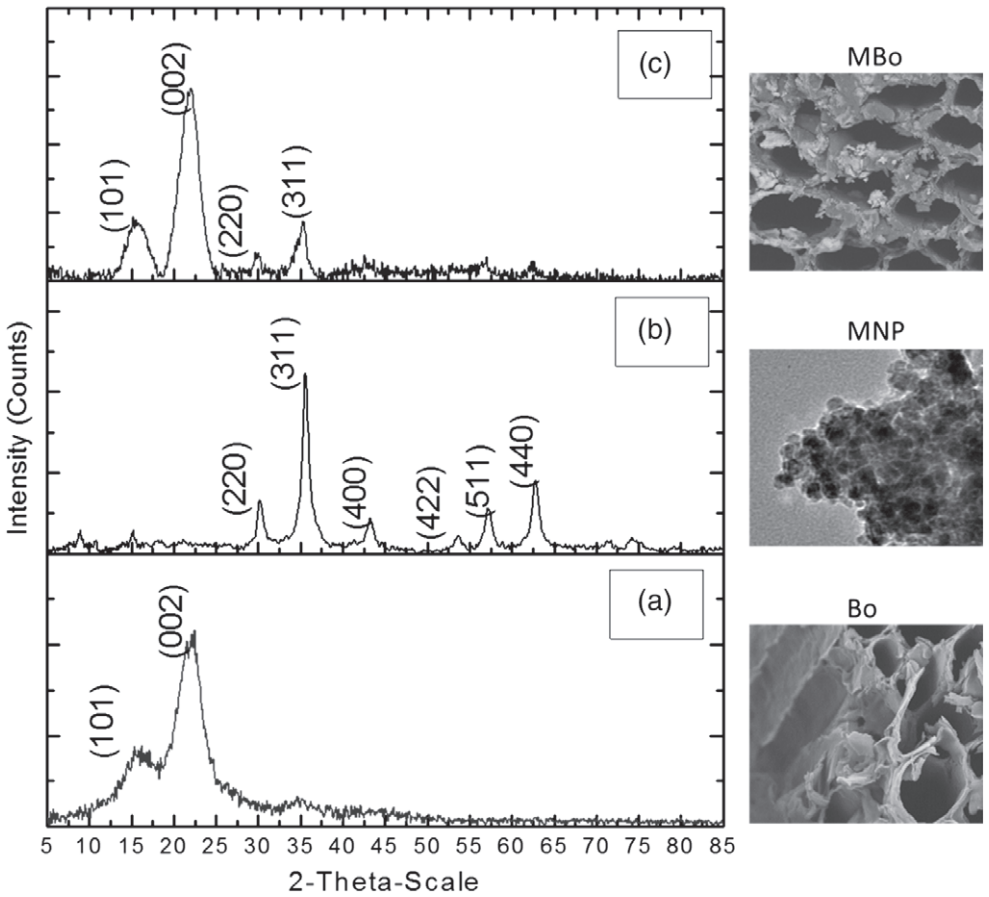

Figure 4. (a) XRD patterns of bagasse (Bo), (b) MNP and (c) MB_O. The inset of each pattern shows a representative SEM image of Bo, MNP and MB_O, respectively.

Method I for Method II, we aimed to produce a material with sufficient magnetic response to be removed by a magnetic field after the process while reducing the cost of synthesis. For the same purpose, the concentrations of Method I were kept the same but the mass of SCB for modification was doubled. The color of the resulting MB_O from methods I and II was black, revealing a higher quantity of nanoparticles than that from Method III. Magnetic response of MB_O from Method III was not as expected and thus, taking into consideration the desorption of Fe from each material, it was decided to use only the MB_O from Method I.

Desorption of Fe as a function of time

Evaluating the amount of Fe desorbed during the process is important, as the maximum permissible Fe concentration for water discharge to the public sewer system is 25 mg L^{-1}.[42] If Fe desorption exceeds this limit, then the process would not be environmentally friendly as Fe would be a new source of water pollution. This also is a significant parameter in case of material regeneration and reuse.

Figure 1 shows desorption of Fe over time from magnetic composites synthesized by three different methods. The Fe concentration in the solutions gradually rose: after 10 h it remained constant for the materials synthesized by methods I and II, whereas equilibrium was achieved at 4 h for material synthesized by Method III. The concentrations at these points were approximately 7.93, 10.4 and 2.20 mg L^{-1} for methods I, II and III, respectively.

As can be seen, in none of the cases did Fe desorption exceed the allowable limit mentioned above. The material obtained from method III was discarded as candidate for the adsorption experiments, due to it low magnetic response despite this composite showed the lowest desorption of Fe ions. By doubling the SCB mass in Method III, the amount of supported magnetite decreased so that its low magnetic response did not meet the objective of the synthesis.

Desorption of Fe from material from Method II was higher than that from method I, even though the amount of magnetite supported should be lower asconcentrations used were halved. This phenomenon can be attributed to the magnetic characteristics of MNP. When there is a greater number of nanoparticles on the material, they attract each other with greater strength, and desorption of Fe ions decreases. Material synthesized by Method I was thus chosen, based on its visual magnetic response and the analysis of the desorption process. Because it was established that the composite desorbed Fe during the adsorption process, it will be important to perform a more specific study of the material regeneration capabilities as reported for magnetic composites.[43]

Material characterization

Figure 2(a) shows the micrograph of the natural SCB. Morphologically, it is a very heterogeneous material with channels and pores of different sizes and shapes; having had no treatment or pre-wash, blocked pores and closed channels can be observed. In Fig. 2(b), channels and pores are unblocked after treatment with C_2H_5OH, corresponding to B_O. Nanomagnetite on the composite MB_O can be observed outside the channels in Fig. 2(c).

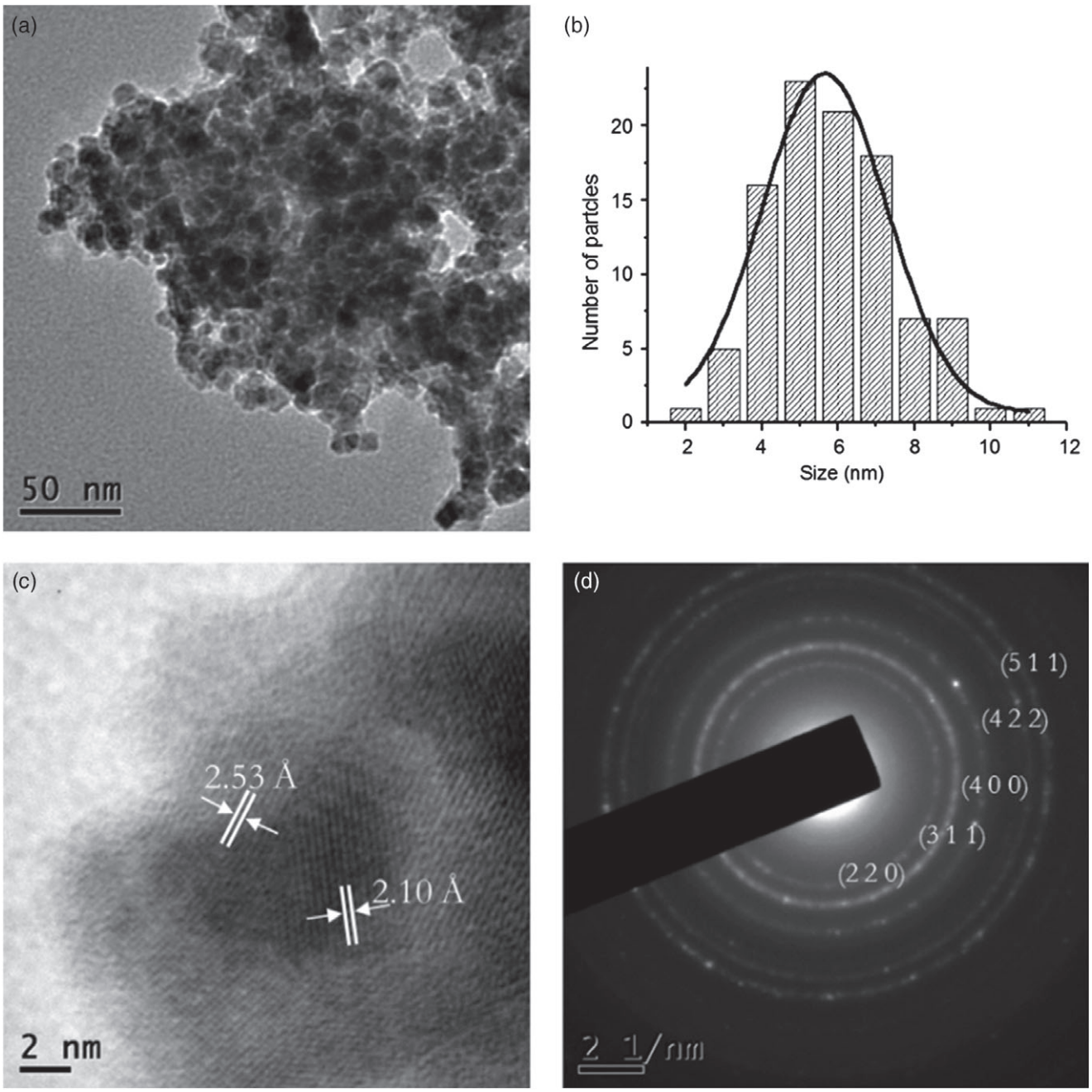

Figure 5. (a) Representative TEM micrograph of the MNP, (b) size distribution histogram of MNP, (c) MNP examined under high-resolution TEM, and (d) their electron diffraction pattern (SAED).

Chemical mapping of Fe shows the distribution of magnetite on SCB in Fig. 2(d).

Figure 3(a) shows the micrograph of MB_O after fluoride adsorption. The composite does not show any significant changes on the surface. The chemical mapping of Fe and fluorine (F) in Fig. 3(b) indicates the distribution of both elements; Fe is represented in red [Fig. 3(c)] and F in green [Fig. 3(d)]. These elements are deposited in different areas on the surface but some interaction between magnetite nanoparticles and fluoride ions are possible, which was confirmed by XPS analysis.

In Fig. 4(a), diffraction peaks at 15.6° and 22.2° are assigned to the reflection from the crystallographic planes (101) and (002) that represent the typical XRD pattern for cellulose or for other lignocellulosic materials. XRD measurement was used to identify the crystalline structure of magnetite nanoparticles. Figure 4(b) shows characteristic peaks at $2\theta = 30$, 35, 43, 54, 57 and 62°, corresponding to (2 2 0), (3 1 1), (4 0 0), (4 2 2), (5 1 1) and (4 4 0) Bragg reflections, respectively (JCPDS card no. 19-0629), which can be indexed on the basis of the inverse cubic spinel structure of magnetite. The absence of the characteristic peaks of maghemite [Fe(II)-deficient magnetite], ranging from a 2θ angle of 20° to 30°, verifies that the main phase corresponds to magnetite.[41] The peaks at 30 and 35° were still observed in the prepared composite MB_O [Fig 4(c)], indicating successful synthesis of magnetite crystals on the SCB surface.

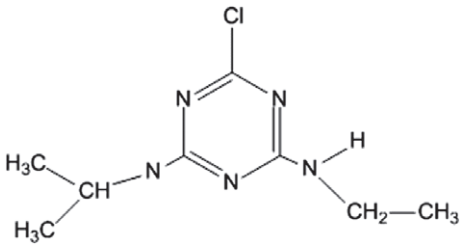

Figure 6. Chemical structure of atrazine.[67]

The Debye–Scherrer equation [Eqn (4)] was used for determining the average crystal particle size of the MNP.[44]

$$D = \frac{K\lambda}{\beta cos\theta} \quad (4)$$

where K is a constant related to the Miller index of crystallographic planes (assigned a value of 0.9), λ is the X-ray wavelength, θ is half the diffraction angle and β is the angular width (in radians) at half-maximum intensity. MNPs had average diameters of *c*. 5 nm, which is in agreement with the results of TEM.

The BET surface area of MB_O was found to be 45.7023 $m^2\ g^{-1}$ with an average pore width of 63.3 nm, and therefore could be classified as a macroporous material. SEM revealed such porosity in the SCB before and after nanoparticle deposition. The total pore volume was 0.047 $cm^3\ g^{-1}$ and in general the material is mesoporous, which allows not only the adsorption of small molecules such as fluoride, but also big ones such as atrazine.

A representative TEM micrograph is shown in Fig. 5(a), where semispherical nanoparticles can be seen. They formed agglomerates despite the fact that MNPs were dispersed by ultrasonication. This behavior is due to the magnetic property of the nanoparticles, which attracted each other. This also was associated to desorption of Fe. Small particles with diameters between 2 and 11 nm were identified [Fig. 5(b)]. High-resolution TEM results confirmed the structural nature of the obtained nanoparticles [Fig. 5(c)]. The lattice spaces of 2.1 and 2.53 Å, according to XRD results, correspond to (400) and (311) Bragg reflection, respectively (JCPDS card no. 19-0629). More details were obtained from selected area electron diffraction (SAED) pattern, inset in Fig. 5(d). It also shows the crystalline nature of MNPs, and the typical crystal structure of magnetite, because interplanar distances and diffraction indexes agreed with the standard JCPDS card no. 19-0629.

Atrazine's chemical structure is showed in Fig. 6. The infrared spectra of B_O is given in Fig. 7(a). The strong signal at 3340 cm^{-1} is typical of cellulose[46] hemicellulose and lignin, corresponding to the presence of stretching vibration –OH.[47] Bands at 2913 cm^{-1} are characteristic of C–H stretching vibration of methyl groups of lignin. The signal, between 1603 and 1608 cm^{-1}, is due to carboxylic groups, present in lignin and hemi-cellulose. Four weak bands around 1450, 1500, 1580 and 1600 cm^{-1} represent the C=C vibration in the aromatic rings of lignin. The strong signal at 1039 cm^{-1} represents the C-O vibration.

In Fig. 7(b) the spectra of MB_O is very similar to the spectra of Bo; however, the signal around 567 cm^{-1} is defined more clearly. This band corresponds to the stretching vibrations of Fe–O bonds, which may suggest the presence of magnetite on the surface of the material.[48]

Figure 7(c) presents the spectra of atrazine. The signal at 3253 cm^{-1} is for the symmetrical N–H stretching vibration that corresponds to the secondary amine groups of isopropyl and ethyl

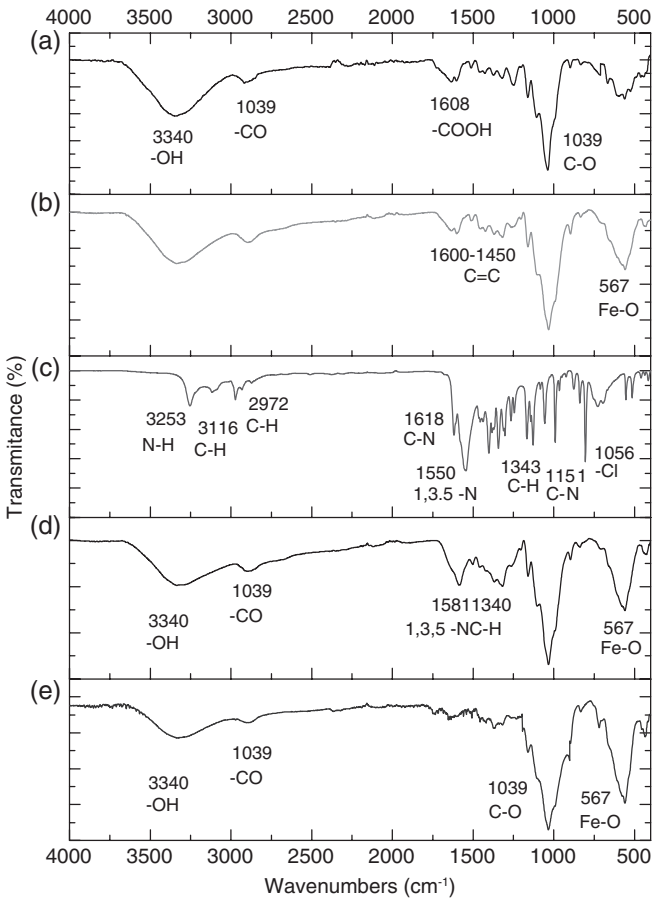

Figure 7. (a) FTIR spectra of bagasse B_O, (b) MB_O, (c) atrazine, (d) MB_O after atrazine adsorption and (e) MB_O bagasse after fluoride adsorption.

side chain. The stretching vibration C–H linked to the amine in the two branched chains is at 3116 cm^{-1}. However, the stretching vibration of C–H corresponding to alkanes is at 2972 cm^{-1}.[49] At 1618 cm^{-1} it is common to find the stretching vibration of C–N. The strong ring-stretching bands at 1550 and 1410 cm^{-1} correspond to three N atoms replacing the 1, 3 and 5 –CH groups in the benzene ring of triazines.[50] At 1343 cm^{-1}, the C–H bending vibration of methyl groups can be seen. The stretching vibration for C–N is at 1151 cm^{-1}. At 1056 cm^{-1} there is a signal related to the aromatic chlorine stretch.

After the adsorption of atrazine in MB_O a small change can be observed around 1581 and 1540 cm^{-1} [Fig. 7(d)]. This slight increase in the signals could be related to the characteristic bands of atrazine. The signals between 2972 and 3253 cm^{-1} corresponding to atrazine are overlapped by the most relevant signals of MB_O. However, not every signal was expected to show up in the spectra because the removal process was established as a chemical adsorption. It means that some changes in the atrazine molecule were expected.

In Fig. 7(e), the MB_O spectra after the adsorption of fluoride was analyzed. According to Mahapatra *et al.*[51] the signal of C–Cl stretching appears from 850 to 550 cm^{-1}. The band in the region 1300–1150 cm^{-1} is associated with the symmetrical stretching of –CF group.[52] Therefore, the chemical sorption of this halogen could be identified in this region but the characteristic signals of the composite MB_O overlap the fluoride signals. However, there are some differences in the intensity and width of the signals

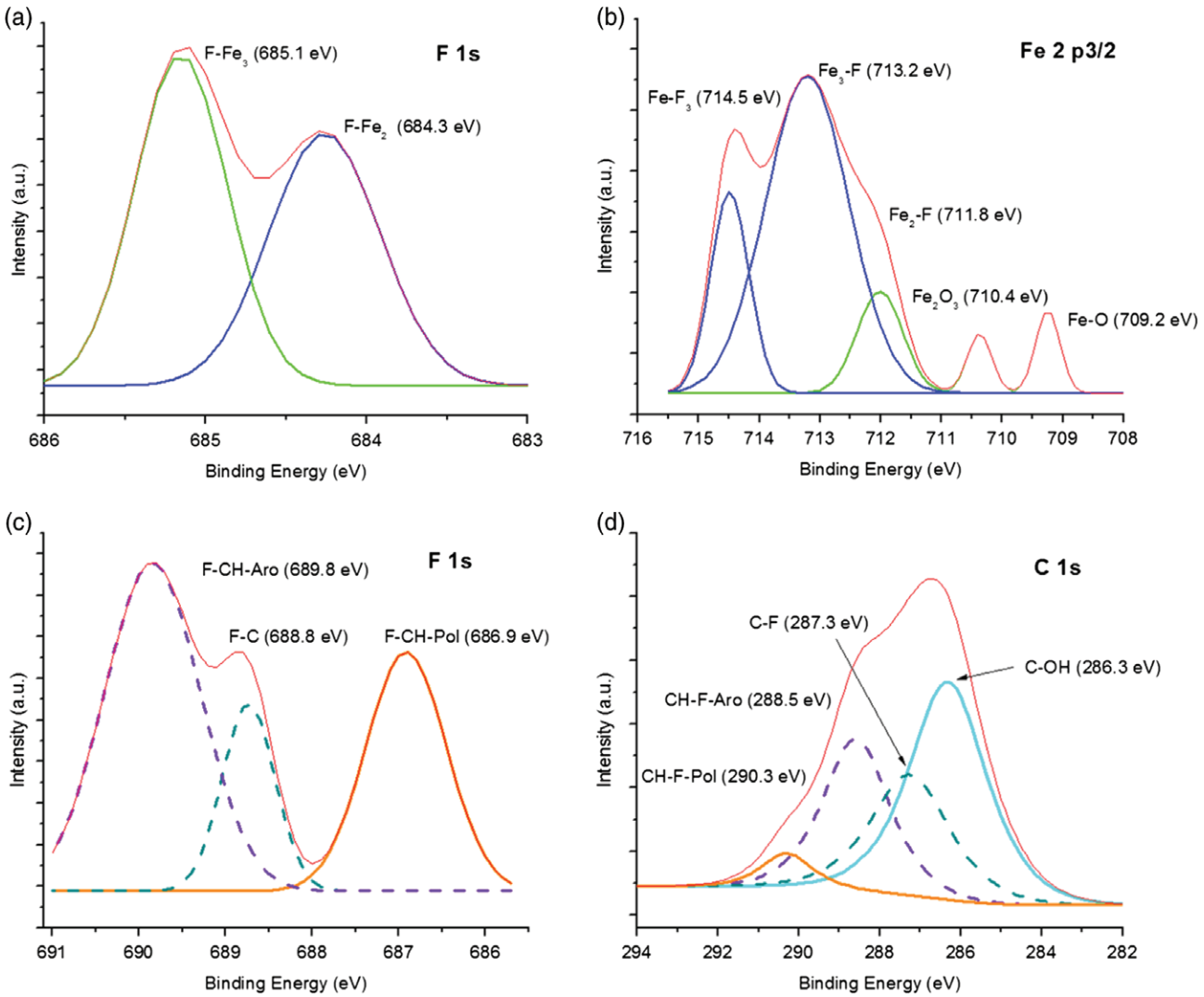

Figure 8. XPS spectra of MB_O after fluoride adsorption: F 1s from 686 to 683 eV (a), F 1s from 691 to 686 eV (b), Fe 2p3/2 (c), and C 1s (d).

at 1039 and 567 cm^{-1} associated with Bo and the Fe–O bond, respectively. They may be attributed to the adsorption of fluoride on the material.

Figure 8 shows XPS spectra of MB_O after fluoride adsorption; Fig. 8(a) and (b) show the F 1s region, after curve-fitting. Two different chemical environments for fluoride resulted; both signals are related to the interaction between Fe and MNPs. These signals result from an interaction of the analyte with the two different oxidation states of Fe, which was something expected because they form part of the magnetite structure. Interactions of F with C, which is the main component of SCB molecules, are visible in Fig. 8(b). Interactions of polymeric chains (Pol) of –CH, aromatic (Aro) –CH and F–C interactions with lignin and cellulose may take place. In order to confirm the interaction signals, curve-fitting expectra of Fe 2p3/2, and C1s are presented in Fig. 8(c) and (d), respectively. In case of Fe 2p3/2 spectra, not only is the signal related to F present, but also characteristics signals of magnetite. For the C 1s region, there are four signals after curve fitting that can be related to the hydroxyl group (C–OH) from SCB, components such as lignin and cellulose, and also three interactions of F with C, which are in good agreement with the signals observed and discussed before in the F 1s region.

Adsorption kinetics

The adsorption kinetics of atrazine on MB_O are illustrated in Fig. 9(a). The adsorption rate in the composite was rapid during the first minutes and equilibrium was achieved at 7 h. The characteristic active sites of the material may have had greater affinity for the pesticide than for the fluoride ions, leading to the high adsorption rate. Atrazine adsorption kinetic parameters of these models are given in Table 1. It can be seen from the statistic values of R^2, RSS and χ^2 that the adsorption process follows the pseudo-second-order model. The best-fitting models suggest that the present adsorption process is a chemisorption involving valence forces through sharing or exchange of electrons[53] between the composite and atrazine molecules. According to the pseudo-second-order model, the process takes place on a very heterogeneous surface. This result was corroborated with the micrographs of SEM and the spectra of FTIR, where an heterogeneous morphology was observed, and many different kinds of functional groups were established.

For the adsorption of fluoride [Fig. 9(b)], the equilibrium time was 6 h, which is faster than when MB_O was applied to remove atrazine. This may indicate that as the fluoride molecule is smaller than the atrazine molecule, it can reach the adsorption sites in

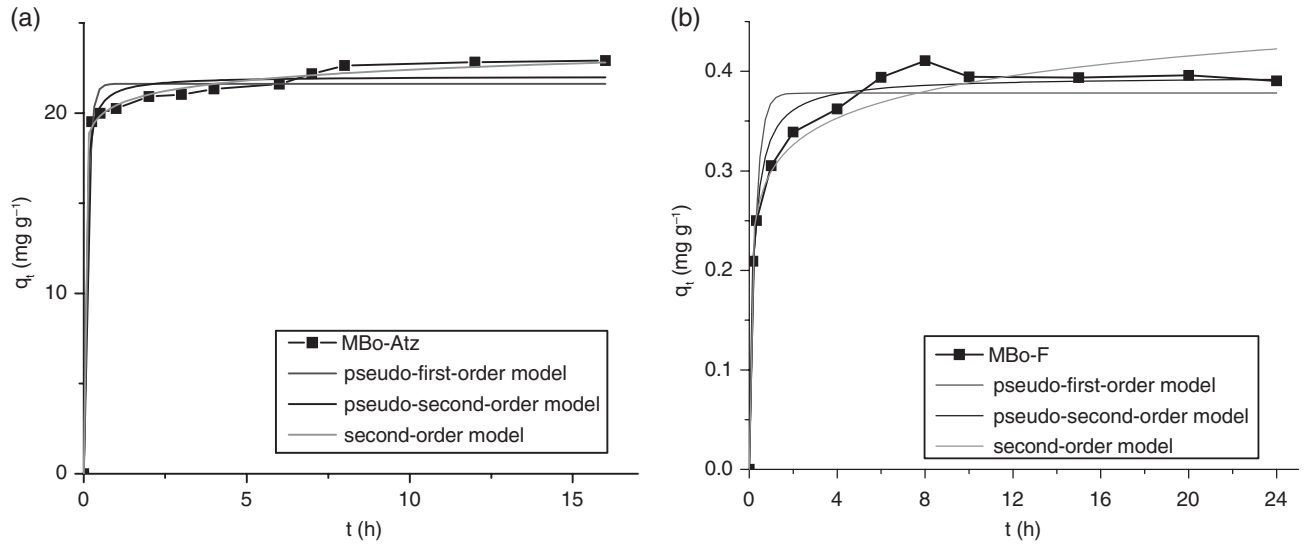

Figure 9. Adsorption kinetics of atrazine (a) and fluoride (b) onto MB_O by using mathematical models (10 mg mass in 5 mL of 30 mg L^{-1} atrazine, not adjusted pH 6.5–7.5, room temperature; 1 g mass in 200 mL of 3 mg L^{-1} of fluoride, not adjusted pH 6.8–7.09, room temperature).

Table 1. Kinetic parameters of atrazine and fluoride adsorption by MB_O

Model[a]	Parameter[b]	Atrazine[c]	Fluoride[c]	Model[a]	Parameter[b]	Atrazine[c]	Fluoride[c]
Pseudo-first-order	q_e	21.63	0.3782	**Pseudo-second-order**	q_e	22.04	0.3950
	k_1	8.774	3.644		k_2	1.083	13.47
	R^2	0.9765	0.9339		R^2	0.9878	0.9807
	RSS	9.226	9.470×10^{-3}		RSS	4.806	2.760×10^{-3}
	X^2	0.9226	9.468×10^{-4}		X^2	0.4806	2.758×10^{-4}
Second-order	α	2.030	86.29				
	β	1.169	25.76				
	R^2	0.9981	0.9726				
	RSS	0.7416	3.920×10^{-3}				
	χ^2	7.416×10^{-2}	3.925×10^{-4}				

[a] Mathematical models applied to isotherm data.
[b] Mathematical parameters from models.
[c] Atrazine removal results from mathematical models.
[d] Fluoride removal results from mathematical models.
q_e, adsorption capacity of the adsorbent at equilibrium time t (mg g^{-1});
k_1, constant rate coefficients for the pseudo-first-order model (h^{-1}).
k_2, constant rate coefficients for the pseudo-second-order model (g mg^{-1} h^{-1}).
α, initial adsorption rate (mg g^{-1} h^{-1}).
β, activation energy for chemisorption (mg g^{-1}).

less time. Fluoride spreads faster toward the adsorption sites of the material than atrazine by the size of molecules. After the application of the mathematical models as mentioned above, it was determined that the systems is best described with the pseudo-second-order model (Table 1), pointing out that the adsorption process was a chemisorption.

Adsorption isotherm

The adsorption isotherms of atrazine and fluoride removal [Fig. 10(a) and (b)] were built at the equilibrium time. Adsorption capacities were established using the model of Langmuir because it is based on the idea of a homogenous monolayer surface phase. The equilibrium factor R_L calculated with the initial concentration and the Langmuir constant indicates unfavorable adsorption if $R_L > 1$, favorable if $0 < R_L < 1$, and irreversible if $R_L = 0$.[54] The value for atrazine adsorption is 0.24 and 0.70 for fluoride, and therefore the adsorption is favorable in each case.

The Freundlich model describes an adsorption process in multilayers on heterogeneous surfaces, where interactions of adsorbed molecules can take place.[55] The Sip (Langmuir–Freundlich) isotherm is more suitable to explain the adsorption process on a heterogeneous surface. It predicts the Freundlich isotherm at low adsorbate concentrations, and the monolayer adsorption capacity of the Langmuir isotherm at high concentrations.[56] This model better predicted the adsorption behavior of atrazine and fluoride on MB_O. Statistics parameters fit better with this model and the characterization of the composite presumes its heterogeneous nature. The Temkin isotherm is an extension of the Langmuir model, which considers variations in the enthalpy of adsorption.[57] Due to adsorbate–adsorbent interactions the energy of the adsorption decreases linearly.[54] The Dubini–Radushkevich model assumes

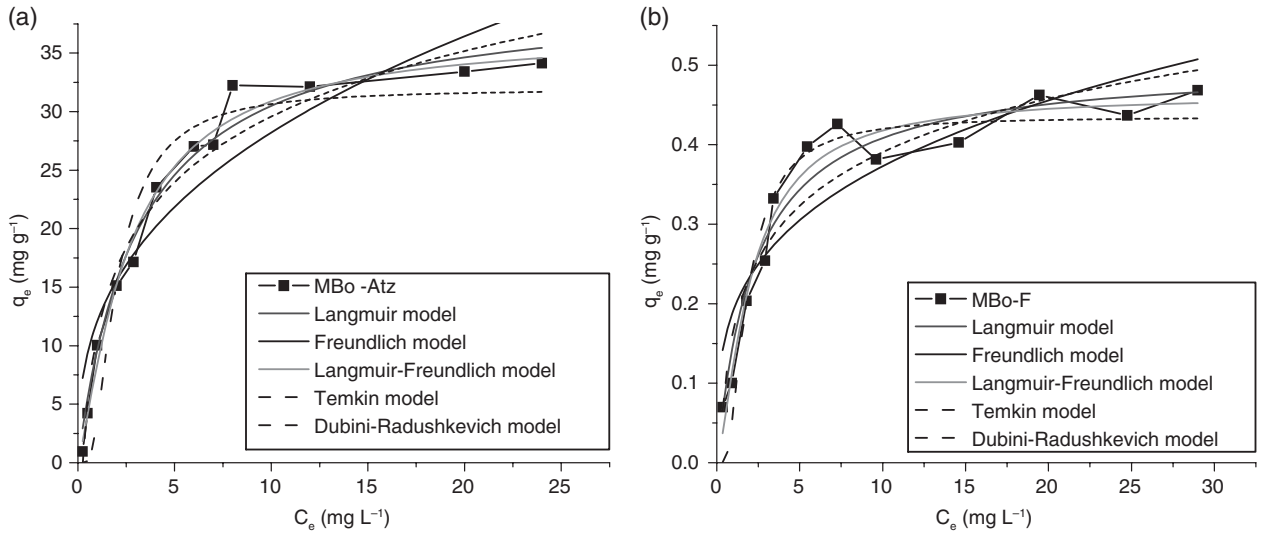

Figure 10. Isotherms of atrazine (a) and fluoride (b) onto MB_O by using mathematical models (10 mg mass in 5 mL of 10–100 mg L^{-1} atrazine, not adjusted pH 6.5–7.5, room temperature; 1 g mass in 200 mL of 1–30 mg L^{-1} of fluoride, not adjusted pH 6.8–7.09, room temperature).

Table 2. Isotherms parameters of atrazine and fluoride adsorption by MB_O

Model[a]	Parameter[b]	Atrozine[c]	Fluoride[c]	Model[a]	Parameter[b]	Atrozine[c]	Fluoride[c]
	q_m	40.11	0.5036	**Temkin**	A	3.880	5.585
	K_L	0.3167	0.4290		B	8.083	9.710×10^{-2}
Langmuir	R^2	0.9804	0.9489		R^2	0.9665	0.9076
	RSS	26.92	9.800×10^{-3}		RSS	45.96	1.784×10^{-2}
	χ^2	2.692	9.876×10^{-4}		χ^2	4.596	1.780×10^{-3}
	q_m	36.80	0.4638	**Dubini–Radushkevich**	q_m	31.92	0.4351
	K	0.2964	0.3666		B_D	7.321×10^{-7}	6.362×10^{-7}
	$1/n$	0.8025	0.7180		E	1.168	1.253
Langmuir–Freundlich	R^2	0.9850	0.9569		R^2	0.9240	0.9215
	RSS	18.51	7.500×10^{-3}		RSS	104.3	1.516×10^{-2}
	χ^2	2.057	8.332×10^{-4}		χ^2	10.43	1.520×10^{-3}
	$1/n$	0.3690	0.2894				
	K_F	12.06	0.1915				
Freundlich	R^2	0.8717	0.8165				
	RSS	176.0	3.544×10^{-2}				
	χ^2	17.60	3.540×10^{-3}				

[a] Mathematical models applied to isotherm data;
[b] Mathematical parameters from models.
[c] Atrazine removal results from mathematical models.
[d] Fluoride removal results from mathematical models.
q_m, maximum adsorption capacity (mg g^{-1}).
K_L, K, K_F: Langmuir, Langmuir–Freundlich, Freundlich constants (L mg^{-1}).
$1/n$, adsorption intensity constant.
A, Temkin binding constant.
B, heat of adsorption (J mol^{-1}).
B_D, Dubinin–Radushkevich isotherm constant (mol^2 J^{-2}).
E, adsorption energy (kJ mol^{-1}).
R^2, Correlation coefficient.
RSS, residual sum of squares.
χ^2, reduced chi-square.

that the adsorption mechanism is carried out with a Gaussian distribution of energy over an heterogeneous surface. It is applied to distinguish between a chemisorption and a physisorption.[58]

Calculated parameters for Langmuir, Freundlich, Langmuir–Freundlich, Temkin and Dubini–Radushkevich models are given in Table 2. The best-fitting model for the removal of atrazine onto MB_O was Langmuir–Freundlich. This model is a versatile isotherm expression that can simulate both Langmuir and Freundlich behaviors.[59] The dimensionless heterogeneity factor $1/n$ describes the heterogeneity of the material because 0.8025 is between 0 and 1. The value of $1/n < 1$ is related to the adsorption intensity constant that varies with the heterogeneity of the adsorbate.[60] The adsorptive capacity was 40.11 mg g^{-1} for the removal of atrazine onto MBo. There are no previous reports of

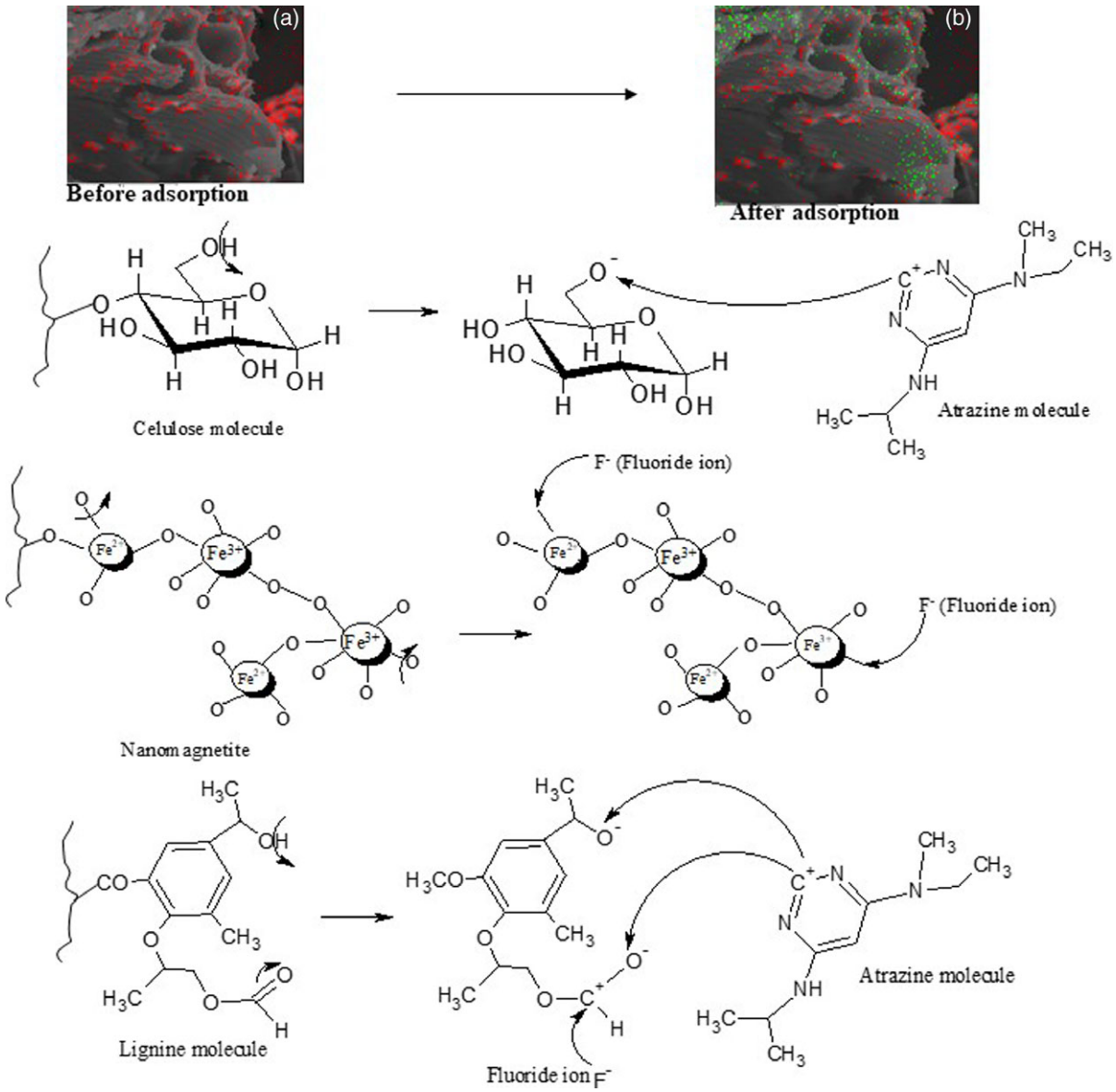

Figure 11. Scheme for the adsorption mechanism of atrazine and fluoride by MB_O. Insets a and b correspond to EDS chemical mapping of MB_O before and after the F adsorption, respectively.

the removal of atrazine with this kind of composite; however, with another magnetic composite Castro *et al.* reported a q_{max} of 25 mg g^{-1}.[61] They reported that the atrazine adsorption capacity diminishes as the content of Fe in the composites increases, maybe because the impregnation with Fe oxide reduced the surface area by its deposition in the activated C pores. In our case, as can be seen in the characterization of the material, the magnetite does not block the pores of the bagasse.

According to Table 2, the best adjusted to the experimental data obtained for MB_O in the adsorption of fluoride was for the Langmuir–Freundlich model. Therefore, the adsorption took place through a heterogeneous surface and the dimensionless heterogeneity factors 1/*n* are between 0 and 1 (0.7180). The Langmuir adsorption model has been broadly used to estimate the adsorption capacity of several elements and chemical species.[62] This allowed establishing a capacity of 0.5036 mg g^{-1}.

In comparison to other research, the fluoride adsorption capacity of MB_O obtained herein is low. Dhillon *et al.*[63] determined an adsorption capacity of 194 mg g^{-1} for a novel Ce–Zn binary metal oxide adsorbent and Wu *et al.*[64] reported 32.310 mg g^{-1} when using a hybrid adsorbent fabricated with Mg/Fe composite oxide and alginate. A more similar material to that explored in the present paper was tested by Jayarathna.[32] They synthesized nanoparticles of maghemite by the co-precipitation method and found that the fluoride removal capacity was 3.65 mg g^{-1}, and that it strongly depended on initial pH of solutions. Singh *et al.*[21] reported that, SCB removed fluoride from aqueous solution with a maximum adsorption capacity of 4.12 mg g^{-1}. According to this reference, and fluoride adsorption results in the present work, MNP diminishes the adsorption capacity of the support material, which can be attributed to the fact that the nanoparticles would be occupying active sites. Therefore, the tested materials may only be applied as adsorbent materials for low concentrations of fluoride. In order to understand this behavior a more detailed study is planned in a forthcoming work.

The atrazine removal capacity of MB_O is higher than data reported for other adsorbent materials including activated peanut husk (4.11 mg g^{-1})[31] and biochars produced from soya beans (1.38 mg g^{-1}).[65] However, Lladó *et al.*[66] determined the adsorption capacity of three different activated Cs, two of them commercial with higher adsorption capacity (212.26 and 119.45 mg g^{-1}). Nevertheless, the third was a sludge-based activated C with an adsorption capacity of 45.49 mg g^{-1}, similar to the MB_O composite.

According to results obtained from mathematical models of kinetics and isotherms of adsorption, as well as the identification of functional groups of the material characterization by FTIR and chemical environment of F from XPS results, a mechanism of adsorption for F and atrazine was proposed (Fig. 11).

The composite has a greater affinity with atrazine than with fluoride. Perhaps to improve the removal of fluoride other elements should be incorporated to the composite to increase fluoride affinity.

CONCLUSIONS

Magnetite is a well-known mineral whose magnetic properties render its efficiency in adsorption processes, because it would facilitate its separation from the system once used for contaminant removal. The affinity of the MB_O composite towards atrazine is greater than with fluoride. The equilibrium times are related to the rate constants in each best-fitted model. Both processes of adsorption were carried out by a chemisorption, which means that the adsorbate removed would be confined within the composite. The adsorption capacities varied, but the highest was obtained for the composite MB_O and the removal of the pesticide. The adsorption capacity to remove fluoride was < 1 mg g^{-1}. However, its characteristics would allow the material to be used for fluoride removal in water containing low concentrations of this contaminant.

The synthesis of the magnetic composite is simple, facilitating mass production, and generates a material easy to manipulate and easy to isolate after the process. It is a novel material that has not yet been tested for the removal of these types of contaminants. As Fe desorption during the adsorption process did not exceed the maximum permissible concentration for water discharge, the composite MB_O can be considered to be environmentally friendly and important adsorbent material in larger scale processes.

ACKNOWLEDGEMENTS

The authors are grateful to Rosa Lina Tovar and Claudia Hernández (Universidad Autónoma de San Luis Potosí, Institute of Metallurgy) for XRD analyses, Lizbeth Triana (CCIQS UAEM-UNAM) for FTIR analysis and Ruth Georgina Salinas for the atomic absorption spectroscopy analysis. This work was supported by CONACYT (Grant No. 280518). The author Toledo-Jaldin thanks to CONACYT for the Grant No. 4497.

REFERENCES

1 Ali A, Zafar H, Zia M, Ul Haq I, Phull AR, Ali JS *et al.*, Synthesis, characterization, applications, and challenges of iron oxide nanoparticles. *Nanotechnol Sci Appl* **9**:49–67 (2016).
2 Onyenwoke RU and Wiegel J, Structure, properties, microbiology and applications of magnetite, in *Magnetite: Structure, Properties and Applications*, ed. by Nova DM. Nova Science Publishers, New York, pp. 297–316 (2011).
3 Grosu Y, Faik A, Ortega-Fernández I and D'Aguanno B, Natural Magnetite for thermal energy storage: excellent thermophysical properties, reversible latent heat transition and controlled thermal conductivity. *Solar Energy Mater Solar Cells* **161**:170–176 (2017).
4 Noval VE, Ochoa Puentes C and Carriazo JG, Magnetita (Fe3O4): una estructura inorgánica con múltiples aplicaciones en catálisis heterogénea. *Rev Colomb Quim* **46**:42–59 (2017).
5 Helber H, Yamaura M and de Sousa JS. *Synthesis of Magnetite Nanoparticles by Microwave Irradiation and Characterization in Seventh International Latin American Conference on Powder Technology*, São Paulo (2009).
6 Unsoy G, Gunduz U, Oprea O, Ficai D, Sonmez M, Radulescu M *et al.*, Magnetite: from synthesis to applications. *Curr Top Med Chem* **15**:1622–1640 (2015).
7 Patel SC, Khalkho R, Patel SK, Sheikh JM, Behera D, Chaudhari S *et al.*, Fluoride contamination of groundwater in parts of eastern India and a preliminary experimental study of fluoride adsorption by natural haematite iron ore and synthetic magnetite. *Environ Earth Sci* **72**:2033–2049 (2014).
8 Azcona P, Zysler R and Lassalle V, Simple and novel strategies to achieve shape and size control of magnetite nanoparticles intended for biomedical applications. *Colloids Surf A* **504**:320–330 (2016).
9 Al-Sabagh AM, Moustafa YM, Hamdy A, Killa HM, Ghanem RM and Morsi RE, Preparation and characterization of sulfonated polystyrene/magnetite nanocomposites for organic dye adsorption. *Egypt J Petrol* **27**:403–413 (2017).
10 Illés E, Tombácz E, Szekeres M, Tóth IY, Szabó Á *et al.*, Novel carboxylated PEG-coating on magnetite nanoparticles designed for biomedical applications. *J Magn Magn Mater* **380**:132–139 (2015).
11 Sharma RK, Yadav M and Gawande MB, Silica-coated magnetic nano-particles: application in catalysis, in *Ferrites and Ferrates: Chemistry and Applications in Sustainable Energy and Environmental Remediation*, ed. by Sharma VK, Doong R-A, Kim H, Varma RS and Dionysiou DD. American Chemical Society, Washington, DC, pp. 1–38 (2006).
12 Saleh TA, Tuzen M and Sarı A, Magnetic activated carbon loaded with tungsten oxide nanoparticles for aluminum removal from waters. *J Environ Chem Eng* **5**:2853–2860 (2017).
13 Saleh TA, Tuzen M and Sarı A, Polyamide magnetic palygorskite for the simultaneous removal of Hg(II) and methyl mercury; with factorial design analysis. *J Environ Manage* **211**:323–333 (2018).
14 Zhang F, Song Y, Song S, Zhang R and Hou W, Synthesis of magnetite–graphene oxide-layered double hydroxide composites and applications for the removal of Pb(II) and 2,4-dichlorophenoxyacetic acid from aqueous solutions. *ACS Appl Mater Interfaces* **7**:7251–7263 (2015).
15 Tuzen M, Sarı A and Saleh TA, Response surface optimization, kinetic and thermodynamic studies for effective removal of rhodamine B by magnetic AC/CeO 2 nanocomposite. *J Environ Manage* **206**:170–177 (2018).
16 Saleh TA and Al-Absi AA, Kinetics, isotherms and thermodynamic evaluation of amine functionalized magnetic carbon for methyl red removal from aqueous solutions. *J Mol Liq* **248**:577–585 (2017).
17 Saleh TA, Tuzen M and Sarı A, Polyethylenimine modified activated carbon as novel magnetic adsorbent for the removal of uranium from aqueous solution. *Chem Eng Res Des* **117**:218–227 (2017).
18 Bhatnagar A and Sillanpää M, Utilization of agro-industrial and municipal waste materials as potential adsorbents for water treatment – a review. *Chem Eng J* **157**:277–296 (2010).
19 Amanda P, Yamamura G and Yamaura M, *Preparation and Evaluation of Adsorption Properties of the Magnetic Bagasse,* INAC 2007, International Nuclear Atlantic Conference, Santos, SP, Brazil (2007).
20 Homagai PL, Ghimire KN and Inoue K, Adsorption behavior of heavy metals onto chemically modified sugarcane bagasse. *Bioresour Technol* **101**:2067–2069 (2010).
21 Singh K, Lataye DH and Wasewar KL, Removal of fluoride from aqueous solution by using low-cost sugarcane bagasse: kinetic study and equilibrium isotherm analyses. *J Hazard Toxic Radioact Waste* **20**:04015024 (2016).
22 Saad SA, Isa KM and Bahari R, Chemically modified sugarcane bagasse as a potentially low-cost biosorbent for dye removal. *Desalination* **264**:123–128 (2010).
23 Sivasankar V, Darchen A, Omine K and Sakthive R, Fluoride: a world ubiquitous compound, its chemistry, and ways of contamination, in *Surface Modified Carbons as Scavengers for Fluoride from Water*. Springer, Cham, pp. 5–32 (2016).
24 Kiran KD, Patterns and distribution of dental caries and dental fluorosis in areas with varying degrees of fluoride ion concentration in drinking water. *J Oral Hyg Health* **1**:108 (2013).

25 Hansen AM, Treviño-Quintanilla LG, Márquez-Pacheco H, Villada-Canela M, González-Márquez LC, Guillén-Garcés R *et al.*, Atrazina: un herbicida polémico. *Rev Int Contam Ambie* **29**:65–84 (2013).
26 Sagarkar S, Gandhi D, Devi SS, Sakharkar A and Kapley A, Atrazine exposure causes mitochondrial toxicity in liver and muscle cell lines. *Indian J Pharmacol* **48**:200–207 (2016).
27 Winchester PD, Huskins J and Ying J, Agrichemicals in surface water and birth defects in the United States. *Acta Paediatr* **98**:664–669 (2009).
28 Ochoa-Acuña H, Frankenberger J and Carbajo C, Drinking-water herbicide exposure in Indiana and prevalence of small-for-gestational-age and preterm delivery. *Environ Health Perspect* **117**:1619–1624 (2009).
29 de la Casa-Resino I, Valdehita A, Soler F, Navas JM and Pérez-López M, Endocrine disruption caused by oral administration of atrazine in European quail. *Comp Biochem Physiol C Toxicol Pharmacol* **156**:159–165 (2012).
30 Wang X, Li J, Xing H and Xu S, Review of toxicology of atrazine and chlorpyrifos on fish. *J Northeast Agric Univ* **18**:88–92 (2011).
31 Saha A, Bhaduri D, Pipariya A and Ghosh RK, Linear and nonlinear sorption modelling for adsorption of atrazine onto activated peanut husk. *Environ Prog Sustain Energy* **36**:348–358 (2017).
32 Jayarathna L, Bandara A, Ng WJ and Weerasooriya R, Fluoride adsorption on $\gamma - Fe_2O_3$ nanoparticles. *J Environ Health Sci Eng* **13**:1–10 (2015).
33 Jiang H, Li X, Tian L, Wang T, Wang Q, Niu P *et al.*, Defluoridation investigation of Yttrium by laminated Y-Zr-Al tri-metal nanocomposite and analysis of the fluoride sorption mechanism. *Sci Total Environ* **648**:1342–1353 (2019).
34 Chen P, Wang T, Xiao Y, Tian E, Wang W, Zhao Y *et al.*, Efficient fluoride removal from aqueous solution by synthetic FeMgLa tri-metal nanocomposite and the analysis of its adsorption mechanism. *J Alloys Compd* **738**:118–129 (2018).
35 Ajala OJ, Nwosu FO and Ahmed RK, Adsorption of atrazine from aqueous solution using unmodified and modified bentonite clays. *Appl Water Sci* **8**:214 (2018). https://doi.org/10.1007/s13201-018-0855-y.
36 Akpinar I and Yazaydin A, Adsorption of atrazine from water in metal–organic framework materials. *J Chem Eng Data* **63**:2368–2375 (2018).
37 Dewage NB, Liyanage AS, Pittman JCU, Mohan D and Mlsna T, Fast nitrate and fluoride adsorption and magnetic separation from water on α-Fe_2O_3 and Fe_3O_4 dispersed on Douglas fir biochar. *Bioresour Technol* **263**:258–265 (2018).
38 Ali I, Alothman ZA and Al-Warthan A, Sorption, kinetics and thermodynamics studies of atrazine herbicide removal from water using iron nano-composite material. *Int J Environ Sci Technol* **13**:733–742 (2016).
39 Rashed MN, Adsorption technique for the removal of organic pollutants from water and wastewater, in . https://www.intechopen.com/books/organic-pollutants-monitoring-risk-and-treatment [18 August 2017].
40 Yu JX, Wang LY, Chi RA, Zhang YF, Xu ZG and Guo J, Competitive adsorption of Pb^{2+} and Cd^{2+} on magnetic modified sugarcane bagasse prepared by two simple steps. *Appl Surf Sci* **268**:163–170 (2013).
41 Mohseni-Bandpi A, Kakavandi B, Rezaei Kalantary R, Azari A and Keramati A, Development of a novel magnetite-chitosan composite for the removal of fluoride from drinking water: Adsorption modeling and optimization. *RSC Adv* **5**:73279–73289 (2015).
42 Food and Agriculture Organization of the United Nations FAO. http://extwprlegs1.fao.org/docs/pdf/ecu112180.pdf Decreto N° 3.516 – Norma de Calidad Ambiental y de descarga de efluentes: recurso agua (Anexo I, Libro VI: De la Calidad Ambiental, del Texto Unificado de la Legislación Secundaria del Ministerio del Ambiente). Source: Registro Oficial Edición Especial [26 August 2018].
43 Adio SO, Asif M, Mohammed ARI, Baig N, Al-Arfaj AA and Saleh TA, Poly (amidoxime) modified magnetic activated carbon for chromium and thallium adsorption: statistical analysis and regeneration. *Process Saf Environ Prot* **121**:254–62 (2018). https://doi.org/10.1016/j.psep.2018.10.008.
44 Kumari M, Pittman CU and Mohan D, Heavy metals [chromium (VI) and lead (II)] removal from water using mesoporous magnetite (Fe_3O_4) nanospheres. *J Colloid Interface Sci* **442**:120–132 (2014).
45 Peat TS, Newman J, Balotra S, Lucent D, Warden AC and Scott C, The structure of the hexameric atrazine chlorohydrolase AtzA. *Acta Crystallogr D Biol Crystallogr* **71**:710–720 (2015).
46 Brandão PC, Souza TC, Ferreira CA, Hori CE and Romanielo LL, Removal of petroleum hydrocarbons from aqueous solution using sugarcane bagasse as adsorbent. *J Hazard Mater* **175**:1106–1112 (2010).
47 Saleh TA, Mercury sorption by silica/carbon nanotubes and silica/activated carbon: a comparison study. *J Water Supply Res Technol* **64**:892–903 (2015).
48 Liu H, Chen W, Liu C, Liu Y and Dong C, Magnetic mesoporous clay adsorbent: Preparation, characterization and adsorption capacity for atrazine. *Microporous Mesoporous Mater* **194**:72–78 (2014).
49 Saleh TA, Isotherm, kinetic, and thermodynamic studies on Hg(II) adsorption from aqueous solution by silica- multiwall carbon nanotubes. *Environ Sci Pollut Res* **22**:16721–16731 (2015).
50 Lin-Vien D, Colthup NB, Fateley WG and Grasselli JG, *The Handbook of Infrared and Raman Characteristic Frequencies of Organic Molecules*. Academic Press Limited, London, pp. 277–306 (1991).
51 Mahapatra K, Ramteke DS and Paliwal LJ, Production of activated carbon from sludge of food processing industry under controlled pyrolysis and its application for methylene blue removal. *J Anal Appl Pyrolysis* **95**:79–86 (2012).
52 Zhang H, Huang H and Shen PK, Methanol-blocking Nafion composite membranes fabricated by layer-by-layer self-assembly for direct methanol fuel cells. *Int J Hydrogen Energy* **37**:6875–6879 (2012).
53 Marín-Allende MJ, Romero Guzmán E, Ramírez García JJ and Reyes R, Chromium(VI) removal from aqueous medium by maize cane and agave bagasse biomasses. *Part Sci Technol* **35**:704–711 (2016).
54 Ali I, AL-Hammadi SA and Saleh TA, Simultaneous sorption of dyes and toxic metals from waters using synthesized titania-incorporated polyamide. *J Mol Liq* **269**:564–571 (2018).
55 Choi J, Chung J, Lee W and Kim JO, Phosphorous adsorption on synthesized magnetite in wastewater. *J Ind Eng Chem* **34**:198–203. (2015). https://doi.org/10.1016/j.jiec.2015.11.008.
56 Ho YS, Review of second-order models for adsorption systems. *J Hazard Mater* **B136**:681–689 (2006).
57 Pursell CP, Hartshorn H, Ward T, Chandler BD and Boccuzzi F, Application of the Temkin model to the adsorption of CO on Gold. *J Phys Chem C* **115**:23880–23892 (2011).
58 Dada AO, Olalekan AP, Olatunya AM and Dada O, Langmuir, Freundlich, Temkin and Dubinin–Radushkevich isotherms studies of equilibrium sorption of Zn^{2+} unto phosphoric acid modified rice husk. *IOSR J Appl Chem* **3**:38–45 (2012).
59 Abu-Sbeiha KA, Salmana M, Al-Momanib I and El-Eswedc B, Cooperative binding of Cadmium(II) on PVA-Bentonite complex in water. *Der Chemica Sinica* **6**:11–17 (2015).
60 Kumara NR, Hamdan N, Petra M, Tennakoon KU and Ekanayake P, Equilibrium Isotherm Studies of Adsorption of Pigments Extracted from Kuduk-kuduk (*Melastoma malabathricum L.*) Pulp onto TiO2 Nanoparticles. *J Chem* **2014**, Article ID 468975, 6 p. http://dx.doi.org/10.1155/2014/468975. (2014).
61 Castro CS, Guerreiro MC, Goncalves M, Oliveira LC and Anastácio AS, Activated carbon/iron oxide composites for the removal of atrazine from aqueous medium. *J Hazard Mater* **164**:609–614 (2009).
62 Dos Santos VC, De Souza JV, Tarley CR, Caetano J and Cardoso Dragunski D, Copper ions adsorption from aqueous medium using the biosorbent sugarcane bagasse in natura and chemically modified. *Water Air Soil Pollut* **216**:351–359 (2011).
63 Dhillon A, Soni SK and Kumar D, Enhanced fluoride removal performance by Ce–Zn binary metal oxide: adsorption characteristics and mechanism. *J Fluoride Chem* **199**:67–76 (2017).
64 Wu T, Mao L and Wang H, Adsorption of fluoride from aqueous solution by using hybrid adsorbent fabricated with Mg/Fe composite oxide and alginate via a facile method. *J Fluoride Chem* **200**:8–17 (2017).
65 Liu N, Charrua AB, Weng CH, Yuan X and Ding F, Characterization of biochars derived from agriculture wastes and their adsorptive removal of atrazine from aqueous solution: a comparative study. *Bioresour Technol* **198**:55–62 (2015).
66 Lladó J, Lao-Luque C, Ruiz B, Fuente E, Solé-Sardans M and David Dorado A, Role of activated carbon properties in atrazine and paracetamol adsorption equilibrium and kinetics. *Process Saf Environ Prot* **95**:51–59 (2015).
67 Peat TS, Newman J, Balotra S, Lucent D, Warden AC and Scott C, The structure of the hexameric atrazine chlorohydrolase AtzA. *Acta Crystallogr D Biol Crystallogr* **71**:710–720 (2015).

